Asian Journal of Chemistry; Vol. 38, No. 4 (2026), 979-994

ASIAN JOURNAL OF CHEMISTRY

https://doi.org/10.14233/ajchem.2026.35429

Crystal Structure and Spectroscopic Characterisation of (*E*)-*N′*-(2,4-dimethoxybenzylidene)-4-nitrobenzohydrazide (DMNBH): A Combined Experimental and DFT Investigation of its Electronic and NLO Properties

B. SUMATHI[1], V. VIJAYALAKSHMI[2], V. SABARI[1,*], S. SANKAR[3] and N. KANAGATHARA[2]

[1]PG & Research Department of Physics, Marudhar Kesari Jain College for Women(A), Vaniyambadi-637751, India
[2]Department of Physics, Saveetha School of Engineering, Saveetha Institute of Medical and Technical Sciences, Thandalam, Chennai-602105, India
[3]Department of Physics, GRT Institute of Engineering and Technology, GRT Mahalakshmi Nagar, Tiruttani-631209, India

*Corresponding author: E-mail: vrsabari86@gmail.com

Received: 10 December 2025 *Accepted*: 20 February 2026 *Published online*: 8 April 2026 AJC-22319

The hydrazone derivative of (*E*)-*N′*-(2,4-dimethoxybenzylidene)-4-nitrobenzohydrazide (DMNBH) was synthesised and characterised experimentally by using single-crystal X-ray diffraction, FT-IR and UV-Vis spectroscopy. XRD established the molecular configuration and crystal packing, supported by intermolecular interactions. FT-IR analysis confirmed the formation of the azomethine (C=N) group along with methoxy and nitro functional groups. UV-Vis spectroscopy showed characteristic π→π* and n→π* transitions attributed to the donor–acceptor framework of the molecule. Density functional theory (DFT) calculations at the B3LYP/6-311++G (d,p) level optimised the molecular geometry and simulate vibrational frequencies, showing good agreement with experimental FT-IR results. Hirshfeld surface analysis and energy framework calculations quantified intermolecular interactions within the crystal lattice. Frontier molecular orbital (HOMO–LUMO) and MEP, indicating intramolecular charge transfer between the donor and acceptor unit. Natural bond orbital (NBO) analysis confirmed effective charge delocalisation and the calculated first-order hyperpolarizability demonstrated the molecule's nonlinear optical (NLO) response. In addition, molecular docking studies were performed to evaluate the biological affinity of DMNBH, revealing favourable binding interactions with the target protein.

Keywords: Schiff base hydrazone, Single-crystal XRD, Hirshfeld surface, Optical property.

INTRODUCTION

Functionally, the hydrazone unit mediates a push–pull electronic mechanism and serves as an efficient pathway for charge separation [1], thereby tuning electronic transitions, absorption characteristics and nonlinear optical properties [2,3]. Therefore, such hydrazone derivatives have attracted considerable attention for the nonlinear optical applications [4-6].

2,4-Dimethoxybenzylidene (DMB) moiety is an electron rich aromatic system in which *ortho*- and *para*-methoxy substituents enhance π-conjugation and intramolecular charge transfer toward the electron-deficient hydrazone unit. This delocalised electronic framework promotes hydrogen bonding, stabilizes supramolecular assemblies and enables efficient electronic communication within the molecule. Accordingly, 2,4-dimethoxybenzylidene derivatives exhibit versatile interactions with biological targets and other molecular systems and are known for their significant pharmacological activities, including anti-inflammatory, antifungal and anticancer effects [7-10].

Schiff base hydrazone derivative (*E*)-*N′*-(2,4-dimethoxy benzylidene)-4-nitrobenzohydrazide (DMNBH) exhibits a nearly planar molecular framework, where 2,4-dimethoxybenzylidene unit is linked to a 4-nitrobenzohydrazide moiety through an (*E*)-configured imine (C=N) bond. The conjugated hydrazone segment (–C=N–NH–CO–) links two electronically distinct aromatic rings, forming a donor–acceptor system that facilitates intramolecular charge delocalisation and enhances molecular linearity, favouring crystalline material formation. This planar geometry arises from the condensation of a ketone with a hydrazide [11,12]. Furthermore, 4-nitrobenzohydrazide (C-nitro) fragment acts as the electron-accepting unit in DMNBH [13], significantly contributing to intramolecular charge transfer and molecular stability [14]. The hydrazide functionality provides effective hydrogen-bonding sites *via* carbonyl oxygen and amide hydrogens, enabling intra- and intermolecular N–H···O and C–H···O interactions that stabilize the supramolecular packing. Extended conjugation across the aromatic ring, carbonyl group and hydrazide nitrogen enhance the π-delocalisation and charge migration along the molecular axis, making this unit valuable for nonlinear optical and optoelectronic applications [15,16]. Additionally, benzohydrazide derivatives exhibit notable biological activities, including antimicrobial, anti-inflammatory and anticancer effects [17-19], highlighting their dual optoelectronic and pharmacological relevancies.

In this way, the electron-rich 2,4-dimethoxybenzylidene donor and the electron-deficient 4-nitrobenzohydrazide acceptor work together to create a polarised π-conjugated framework that improves electronic communication and stabilizes the molecular system by effectively delocalizing the charge. This arrangement promotes efficient charge migration, increases molecular polarizability and consequently enhances optical nonlinearity [13]. Owing to these features, hydrazone derivatives have emerged as promising candidates for advanced photonic and optoelectronic applications. In this context, Saraswathi *et al.* [20] reported the optoelectronic potential of (*E*)-*N*′-(2,4-dimethoxybenzylidene)benzohydrazide, while Jeeva *et al.* [21] and Arunagiri *et al.* [22] demonstrated significant nonlinear optical responses in related dimethoxy-, fluoro-, bromo- and dihydroxy-substituted benzohydrazide hydrazones. Despite these advances, comprehensive studies correlating structure–property relationships with biological activity remain limited.

This work reports, for the first time, the crystal structure of (*E*)-*N*′-(2,4-dimethoxybenzylidene)-4-nitrobenzohydrazide (DMNBH), investigated using combined experimental and theoretical approaches. SCXRD, FT-IR and UV-Vis spectroscopy were employed to elucidate its structural and optical properties, while DFT calculations at the B3LYP/6-311++G (d,p) level provided optimised geometry, vibrational and electronic insights. NBO, Hirshfeld surface, energy framework and HOMO–LUMO analyses revealed charge delocalisation, intermolecular interactions and charge-transfer characteristics, respectively. The nonlinear optical response was evaluated through first-order hyperpolarizability calculations and molecular docking studies assessed biological affinity.

EXPERIMENTAL

Synthesis: An ethanolic solution of 2,4-dimethoxybenzaldehyde (3.3 g, 0.02 mol) and 3.62 g (0.02 mol) of 4-nitrobenzohydrazide dissolved in ethanol was mixed in 100 mL round bottomed flask. The reaction mixture was refluxed for continuously 2 to 3 h and the completion of the reaction was monitored by thin layer chromatography (TLC). After the reaction mixture was poured into ice cold water, a crude solid was obtained, filtered, washed with water two to three times and dried, then finally washed with diethyl ether and kept in over a vacuum for 2 days (**Scheme-I**). The crude sample was recrystallised from ethanol and DMSO mixture by slow evap-oration technique to afford the desired hydrazone as a crystalline solid (yield: 80%).

X-ray single crystal data collection: A crystal of dimension (0.425 mm × 0.110 mm × 0.054 mm) was sealed in a capillary tube and intensities collected at room temperature 293(2) K using a Bruker D8 Venture diffractometer. The graphite monochromatised Mo*K*α (λ = 0.71073 Å) was used and the face-indexed analytical absorption was calculated using the SHELXL program [23], the maximum and minimum transmission factors being 0.7452 and 0.5199, respectively. About 2791 reflections were collected out of 43600 with independent reflections, R_{int} = 0.0248 were used for structure solution and refinement. The structure was solved by a direct method and subsequent difference Fourier syntheses of SHELXL-PLUS program system [23] and the structure refinement was done by use of SHELXL 97 [24]. The anisotropic displacement parameters were included for all non-hydrogen atoms. The crystal data and structure refinement parameters are given in Table-1.

Measurement of vibrational and UV spectra: The vibrational spectrum of the DMNBH compound was recorded using a Bruker IFS 113V FT-IR spectrometer in the range of 4000-500 cm^{-1}, employing the KBr pellet method to identify the characteristic functional group vibrations and confirm molecular bonding features. The UV-Visible absorption spectrum was obtained in the 280-800 nm region using a Perkin-Elmer Lambda 35 spectrophotometer.

DFT calculations: Quantum chemical calculations were performed using the Gaussian 16 software package [25] to investigate the structural and electronic characteristics of the DMNBH molecule. The B3LYP functional with the 6-311 ++G(d,p) basis set was employed for all geometry optimisations and frequency calculations, confirming a true minimum with no imaginary frequencies. The potential energy distribution (PED) analysis of the compound was then performed using the VEDA program [26]. Time-dependent DFT (TD-DFT) was utilised to analyze the electronic excitation behaviour. Visualisation and molecular property analyses were carried out using GaussView 5.0 [27]. Hirshfeld surface and energy framework analyses were conducted CrystalExplorer [28] to evaluate intermolecular interactions and lattice stabili-

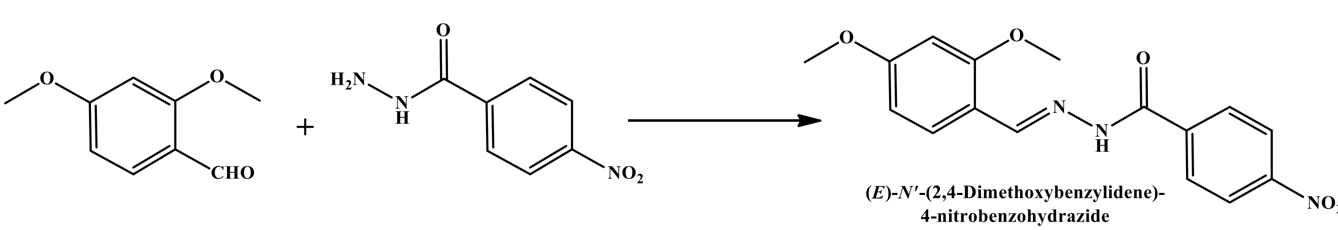

Scheme-I: Synthesis of (*E*)-*N*′-(2,4-dimethoxybenzylidene)-4-nitrobenzohydrazide (DMNBH)

TABLE-1
CRYSTAL DATA OF DMNBH

Temperature	302(±2) K
Formula	$C_{16}H_{15}N_3O_5$
Molecular weight	329.31
Crystal system	Monoclinic
Space group	$P2_1/c$
a (Å)	11.7760(14)
b (Å)	14.6902(14)
c (Å)	9.1275(8)
α (º)	90
β (º)	90.830(4)
γ (º)	90
V (Å^3)	1578.8 (3)
Z	4
F (000)	688
Dcal (g cm^{-1})	1.385
θ range (º)	3.128-25.038
μ (mm^{-1})	0.105
Crystal size (mm)	0.425 × 0.110 × 0.054
T_{min}/T_{max}	0.7452/0.5199
Total/unique/obs refls	9622/4437/2758
R_{int}	0.0207
R [F2>2σ(F2)][a]	0.0609
wR [F2 all refls][a]	0.1616
S	1.038
Δρmax, Δρmin (eÅ^{-3})	+0.195, -0.184

sation energies. FMO, MEP and NBO analyses provided insights into charge distribution and donor–acceptor characteristics. Molecular docking simulations were performed using AutoDock [29] and the docked complexes were visualised in PyMOL [30] to examine the binding orientation and interaction pattern with the selected receptor.

RESULTS AND DISCUSSION

The structural analysis of (*E*)-*N′*-(2,4-dimethoxybenzylidene)-4-nitrobenzohydrazide (DMNBH) confirms that compound crystallizes in the monoclinic crystal system with space group $P2_1/c$, having unit cell parameters a = 11.7760(14) Å, b = 14.6902(14) Å and c = 9.1275(8) Å (Table-1). The asymmetric unit contains a single molecule stabilised by a network of non-covalent interactions. The ORTEP representation (Fig. 1) illustrates that the molecule adopts an E-configuration about the C=N bond, with molecular planarity maintained by an intramolecular N–H···O hydrogen bond between the hydrazide N–H and the carbonyl oxygen. This planar geometry of the –CONH–N=CH– linkage promotes π-conjugation between the aromatic rings, enhancing electronic delocalisation. The optimised structure obtained from density functional theory (DFT) calculations at the B3LYP/6-311++G(d,p) level using the Gaussian 16 package (Fig. 2) closely agrees with the experimental geometry, retaining the coplanar arrangement of the hydrazone bridge and aromatic systems, which validates the consistency between theoretical and crystallographic results. Theoretical bond parameters show excellent correlation with XRD data (Table-2), confirming the reliability of the computational model and the stability of optimised structure. The experimental C=O (C1–O3) and C–N (C1–N2) bond lengths of 1.226(3) Å and 1.344(3) Å align with the

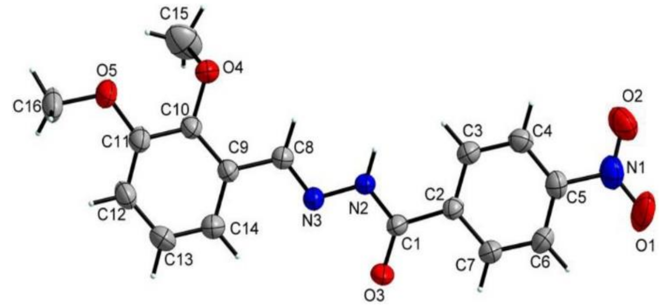

Fig. 1. Molecular structure of DMNBH

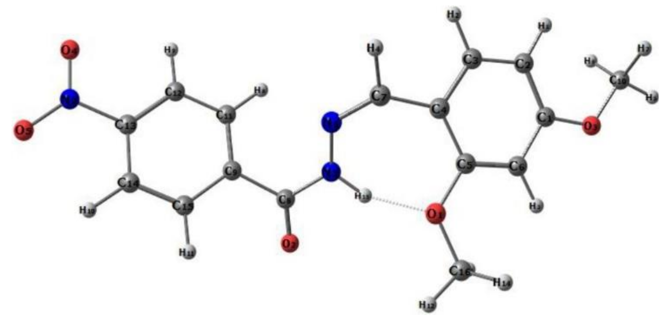

Fig. 2. Optimized structure of DMNBH

DFT values of 1.223 Å and 1.378 Å, indicating partial double-bond character due to conjugation within the hydrazone framework. The N2–N3 bond (1.384(3) Å) confirms the hydrazone linkage, while C8–N3 (1.273(3) Å) represents the azomethine bond. The nitro substituent displays normal geometry with N1–O1 = 1.212(3) Å, N1–O2 = 1.221(3) Å and an O1–N1–O2 angle of 123.7º, consistent with the DFT-calculated value of 124.6º. The methoxy groups exhibit standard C–O bond distances of 1.414(4) Å and 1.423(3) Å, while aromatic C–C distances range between 1.37-1.39 Å with internal angles near 120º, confirming aromatic conjugation and delocalised π-electron density. The O3–C1–N2 (122.6º) and C1–N2–N3 (118.2º) bond angles further support a planar hydrazone core favourable for extended conjugation. The molecular structure of DMNBH is stabilised by both intra and intermolecular hydrogen bonds (Table-3), where the intramolecular N(2)—H(2A)···O (3) hydrogen bond [d(H···O) = 2.098 Å, ∠D–H···A = 161º] forms a six-membered S (6) ring motif locking the molecule in the E-configuration. Intermolecular C–H···O interactions such as C(8)–H(8)···O(3)#1 [d(H···O) = 2.40 Å, ∠D–H···A = 141.1º] and C(15)-H(15 A)···O(2)#2 [d(H···O) = 2.54 Å, ∠D–H···A = 164.9º], further extend the molecular units into chains along the *c*-axis, forming a supramolecular framework. The crystal packing shown in Fig. 3 clearly illustrates the directional hydrogen-bonded chains, while the overall three-dimensional arrangement stabilised by these interactions is displayed in Fig. 4. To support this structural description, the atomic displacement parameters, fractional atomic coordinates and isotropic or equivalent isotropic displacement parameters (Å^2) are summarised in Tables 4 and 5. These intra and intermolecular hydrogen-bonding interactions strengthen the crystal packing and the good agreement between the experimental and DFT results confirms the stable geometry and conjugated structure of the DMNBH molecule.

TABLE-2
BOND LENGTH (Å) AND BOND ANGLE (°) OF DMNBH

Bond length					
Atom	XRD	DFT	Atom	XRD	DFT
C1-O3	1.226(3)	1.22303	C10-C11	1.395(3)	1.3891
C1-N2	1.344(3)	1.37837	C11-O5	1.371(3)	1.35793
C1-C2	1.497(3)	1.50295	C11-C12	1.379(4)	1.39978
C2-C3	1.386(3)	1.39992	C12-C13	1.388(4)	1.3961
C2-C7	1.388(3)	1.40049	C12-H12	0.93	1.08059
C3-C4	1.381(3)	1.39004	C13-C14	1.363(4)	1.4012
C3-H3	0.93	1.07987	C13-H13	0.93	1.08483
C4-C5	1.373(3)	1.39048	C14-H14	0.93	1.08059
C4-H4	0.93	1.08102	C15-O4	1.414(4)	1.42497
C5-C6	1.373(4)	1.3913	C15-H15A	0.96	1.09453
C5-N1	1.478(3)	1.48015	C15-H15B	0.96	1.09458
C6-C7	1.385(4)	1.38822	C15-H15C	0.96	1.08827
C6-H6	0.93	1.08101	C16-O5	1.423(3)	1.43033
C7-H7	0.93	1.08237	C16-H16A	0.96	1.08798
C8-N3	1.273(3)	1.28576	C16-H16B	0.96	1.09316
C8-C9	1.466(3)	1.47933	C16-H16C	0.96	1.09349
C8-H8	0.93	1.08852	N1-O1	1.212(3)	1.22467
C9-C10	1.387(3)	1.4012	N1-O2	1.221(3)	1.22495
C9-C14	1.401(3)	1.41779	N2-N3	1.384(3)	1.36139
C10-O4	1.383(3)	1.35793	N2-H2A	0.847(16)	1.01975
Bond angle					
Atom	XRD	DFT	Atom	XRD	DFT
O3-C1-N2	122.6(2)	119.133	C12-C11-C10	119.7(2)	118.546
O3-C1-C2	120.4(2)	120.83	C11-C12-C13	120.0(2)	120.559
N2-C1-C2	117.04(19)	120.019	C11-C12-H12	120	121.722
C3-C2-C7	119.4(2)	119.557	C13-C12-H12	120	121.722
C3-C2-C1	123.6(2)	123.857	C14-C13-C12	120.5(2)	120.559
C7-C2-C1	117.0(2)	116.446	C14-C13-H13	119.7	118.01
C4-C3-C2	120.6(2)	120.305	C12-C13-H13	119.7	117.722
C4-C3-H3	119.7	119.478	C13-C14-C9	120.5(2)	123.482
C2-C3-H3	119.7	120.216	C13-C14-H14	119.7	118.504
C5-C4-C3	118.6(2)	118.832	C9-C14-H14	119.7	119.73
C5-C4-H4	120.7	119.689	O4-C15-H15A	109.5	111.159
C3-C4-H4	120.7	121.479	O4-C15-H15B	109.5	105.455
C4-C5-C6	122.4(2)	122.094	H15A-C15-H15B	109.5	109.866
C4-C5-N1	119.0(2)	118.924	O4-C15-H15C	109.5	110.637
C6-C5-N1	118.6(2)	118.981	H15A-C15-H15C	109.5	109.525
C5-C6-C7	118.4(2)	118.474	H15B-C15-H15C	109.5	109.866
C5-C6-H6	120.8	119.83	O5-C16-H16A	109.5	111.237
C7-C6-H6	120.8	121.694	O5-C16-H16B	109.46	105.706
C6-C7-C2	120.6(2)	120.716	H16A-C16-H16B	109.5	109.424
C6-C7-H7	119.7	120.429	O5-C16-H16C	109.5	111.242
C2-C7-H7	119.7	118.853	H16A-C16-H16C	109.5	109.424
N3-C8-C9	119.1(2)	134.909	H16B-C16-H16C	109.5	109.714
N3-C8-H8	120.4	111.823	O1-N1-O2	123.7(3)	124.622
C9-C8-H8	120.4	113.073	O1-N1-C5	118.2(3)	117.678
C10-C9-C14	118.9(2)	116.446	O2-N1-C5	118.1(3)	117.7
C10-C9-C8	120.7(2)	115.442	C1-N2-N3	118.19(18)	122.753
C14-C9-C8	120.4(2)	115.442	C1-N2-H2A	123.6(18)	114.166
O4-C10-C9	118.84(19)	116.798	N3-N2-H2A	118.2(18)	119.269
O4-C10-C11	120.7(2)	122.184	C8-N3-N2	116.36(19)	120.957
C9-C10-C11	120.4(2)	121	C10-O4-C15	116.6(2)	118.733
O5-C11-C12	124.4(2)	124.839	C11-O5-C16	117.6(2)	119.841
O5-C11-C10	115.9(2)	115.247			

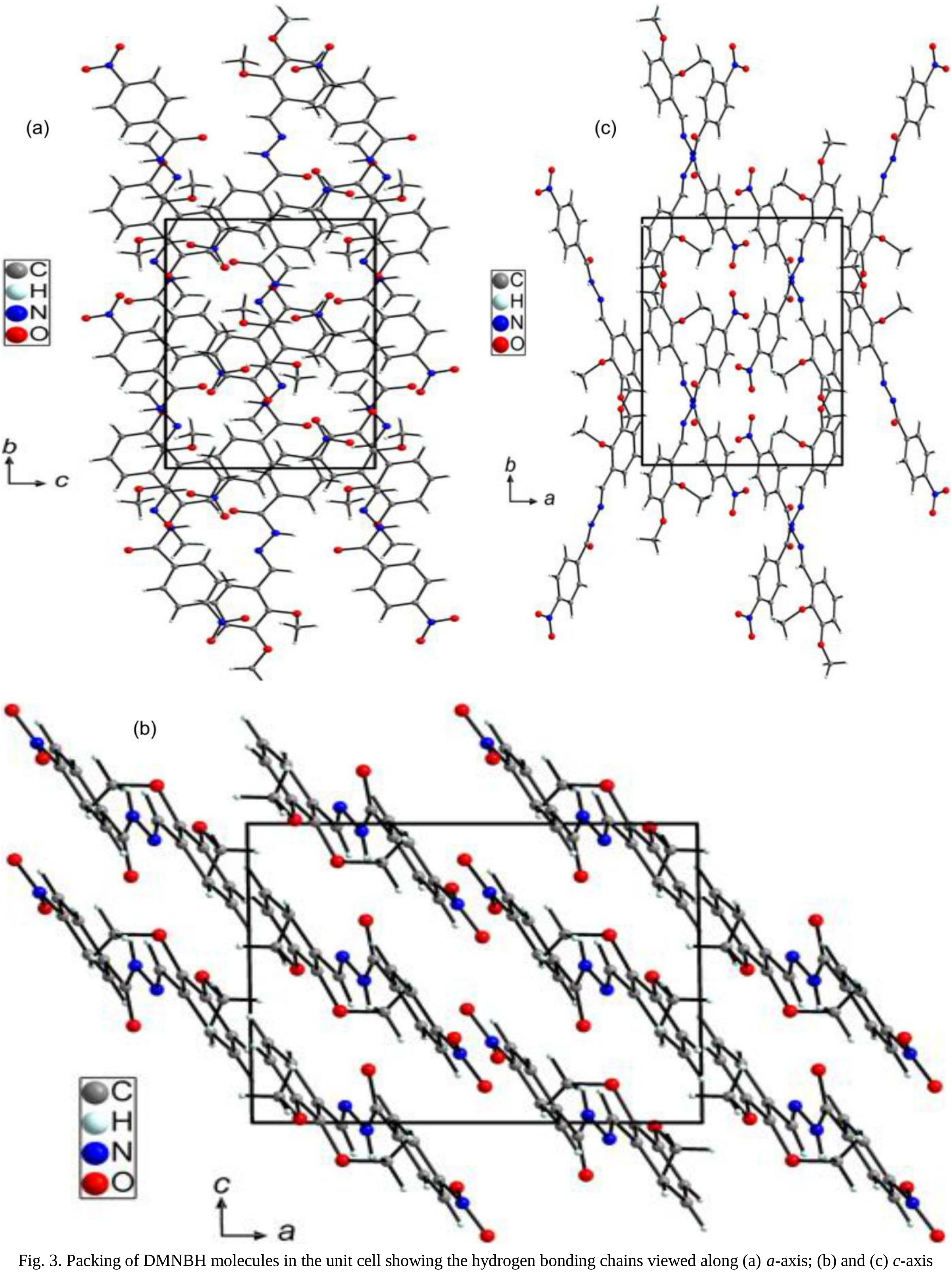

Fig. 3. Packing of DMNBH molecules in the unit cell showing the hydrogen bonding chains viewed along (a) *a*-axis; (b) and (c) *c*-axis

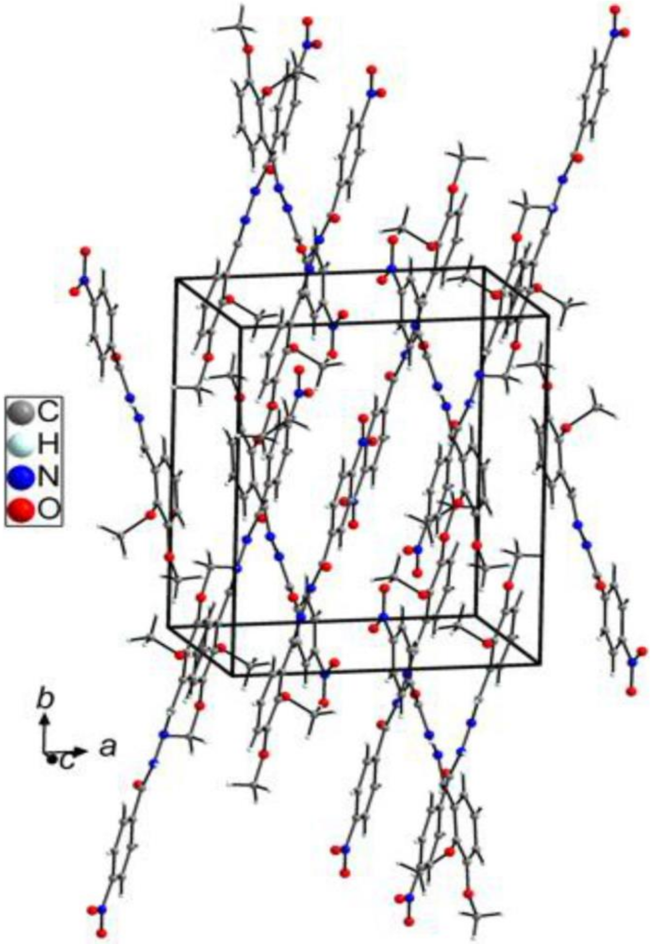

Fig. 4. Three-dimensional packing diagram of DMNBH

TABLE-3
HYDROGEN BONDS OF DMNBH

D–H···A	D–H	H···A	D···A	DHA
C8–H8···O3	0.93	2.4	3.18	141.1(4)
C15–H15A···O2	0.96	2.54	3.477(5)	164.9(4)
C15–H15C···O5	0.96	2.38	2.921(4)	115.5
N2–H2A···O3	0.847(16)	2.098(18)	2.911(2)	161(2)

Hirshfeld surface analysis: The surface characteristics and intermolecular interactions of the DMNBH crystal were analysed using Hirshfeld surface analysis, which defines a boundary where the electron density of molecule equals that of its neighbouring atoms. 3D-Hirshfeld surfaces [31] and two-dimensional fingerprint plots [32] were used to visualize and quantify the size, shape and nature of the intermolecular contacts present within the molecule. Through the d_{norm} mapped surface of DMNBH molecule (Fig. 5a) illustrates the red region on the surface correspond to strong close contacts, primarily associated with the N–H···O and C–H···O hydrogen bonding interactions, confirming these sites as the primary hydrogen bond acceptors within the crystal lattice. The hydrogen atoms attached to the hydrazide nitrogen and aromatic rings serve as donor sites, forming stabilizing contacts with nearby oxygen atoms of neighbouring molecules. The broad blue region and faint white areas represent weak van der Waals interactions around the aromatic rings, contributing to the overall stability and packing efficiency of the crystal structure. In addition, the molecular topology was obtained from shape index and curvedness surfaces (Fig. 6). The shape index surface effectively distinguishes between π···π stacking and void regions through alternating red and blue triangles on the aromatic planes, suggesting the presence of weak π–π and C–H···π

TABLE-4
ATOMIC DISPLACEMENT PARAMETERS (Å^2) of DMNBH

Atom	U11	U22	U33	U23	U13	U12
C1	0.0604(16)	0.0362(13)	0.0364(13)	0.0040(10)	0.0001(11)	-0.0045(11)
C2	0.0487(15)	0.0361(12)	0.0369(12)	0.0025(10)	-0.0043(10)	0.0001(10)
C3	0.0568(16)	0.0412(13)	0.0445(13)	0.0052(11)	0.0028(11)	-0.0019(12)
C4	0.0539(16)	0.0546(16)	0.0475(14)	0.0042(12)	0.0097(12)	0.0024(12)
C5	0.0474(15)	0.0471(14)	0.0552(15)	-0.0080(12)	0.0024(12)	0.0026(11)
C6	0.0741(19)	0.0355(14)	0.0631(17)	0.0060(12)	0.0094(14)	-0.0006(13)
C7	0.0754(19)	0.0417(14)	0.0467(14)	0.0052(12)	0.0135(13)	0.0014(13)
C8	0.0567(16)	0.0399(13)	0.0385(12)	0.0005(11)	0.0024(11)	-0.0001(11)
C9	0.0529(15)	0.0386(13)	0.0370(12)	-0.0025(10)	-0.0002(10)	0.0018(11)
C10	0.0537(15)	0.0414(13)	0.0364(12)	-0.0016(10)	-0.0010(11)	0.0041(11)
C11	0.0656(18)	0.0422(14)	0.0446(13)	-0.0021(11)	-0.0039(12)	0.0090(12)
C12	0.077(2)	0.0553(17)	0.0485(15)	-0.0114(13)	0.0062(13)	0.0141(14)
C13	0.082(2)	0.0640(18)	0.0436(14)	-0.0027(13)	0.0171(14)	0.0013(15)
C14	0.0704(18)	0.0462(15)	0.0448(14)	0.0016(11)	0.0059(12)	-0.0017(13)
C15	0.070(2)	0.129(3)	0.097(3)	-0.014(2)	0.022(2)	-0.022(2)
C16	0.129(3)	0.0450(16)	0.069(2)	-0.0147(14)	-0.0102(19)	0.0237(18)
N1	0.0662(17)	0.0602(17)	0.0825(18)	-0.0137(14)	0.0101(14)	0.0100(13)
N2	0.0685(15)	0.0360(11)	0.0337(10)	0.0022(9)	0.0070(10)	0.0043(10)
N3	0.0624(14)	0.0376(11)	0.0393(11)	-0.0013(9)	0.0023(9)	0.0025(10)
O1	0.140(2)	0.0453(14)	0.169(3)	-0.0111(15)	0.071(2)	0.0068(14)
O2	0.1010(19)	0.0942(17)	0.0782(15)	-0.0105(13)	0.0261(14)	0.0321(14)
O3	0.1235(18)	0.0465(10)	0.0338(9)	0.0050(8)	0.0107(10)	0.0087(10)
O4	0.0759(13)	0.0456(10)	0.0454(10)	0.0040(8)	0.0123(9)	-0.0016(9)
O5	0.1050(17)	0.0406(10)	0.0599(11)	0.0002(9)	0.0068(10)	0.0197(10)

TABLE-5
FRACTIONAL ATOMIC COORDINATES AND ISOTROPIC OR EQUIVALENT ISOTROPIC DISPLACEMENT PARAMETERS (Å^2)

Atom	X	Y	Z	U ISO or EQUI
C1	0.7235(2)	0.81825(15)	0.4549(2)	0.0443(6)
C2	0.6763(2)	0.89428(15)	0.5448(2)	0.0406(6)
C3	0.6209(2)	0.88128(16)	0.6760(3)	0.0475(6)
H3	0.613567	0.822832	0.713846	0.057
C4	0.5764(2)	0.95438(17)	0.7511(3)	0.0519(7)
H4	0.540081	0.945865	0.839862	0.062
C5	0.5868(2)	1.03988(17)	0.6920(3)	0.0499(6)
C6	0.6421(2)	1.05555(17)	0.5629(3)	0.0575(7)
H6	0.649582	1.114287	0.526315	0.069
C7	0.6865(2)	0.98170(16)	0.4887(3)	0.0545(7)
H7	0.723363	0.990772	0.400498	0.065
C8	0.8013(2)	0.59266(16)	0.5099(3)	0.0451(6)
H8	0.774484	0.585561	0.604594	0.054
C9	0.8536(2)	0.51594(15)	0.4335(2)	0.0428(6)
C10	0.8502(2)	0.42889(16)	0.4922(2)	0.0439(6)
C11	0.9014(2)	0.35637(16)	0.4199(3)	0.0508(7)
C12	0.9578(3)	0.37183(19)	0.2909(3)	0.0601(7)
H12	0.992542	0.323793	0.242617	0.072
C13	0.9626(3)	0.45910(19)	0.2330(3)	0.0631(8)
H13	1.001007	0.469309	0.146264	0.076
C14	0.9114(2)	0.52995(17)	0.3024(3)	0.0538(7)
H14	0.914952	0.588064	0.262286	0.065
C15	0.7024(3)	0.3610(3)	0.6299(4)	0.0984(12)
H15A	0.651521	0.378662	0.551813	0.148
H15B	0.665255	0.3684	0.722106	0.148
H15C	0.723639	0.298409	0.617663	0.148
C16	0.9396(3)	0.19667(19)	0.4130(3)	0.0810(10)
H16A	0.908997	0.194396	0.315069	0.121
H16B	0.919785	0.141969	0.464218	0.121
H16C	1.020799	0.201975	0.409616	0.121
N1	0.5360(2)	1.11807(18)	0.7692(3)	0.0696(7)
N2	0.74601(18)	0.73958(13)	0.5246(2)	0.0460(5)
H2A	0.735(2)	0.7314(17)	0.6152(19)	0.055
N3	0.79307(18)	0.66915(13)	0.4451(2)	0.0464(5)
O1	0.5480(3)	1.19332(16)	0.7173(3)	0.1177(11)
O2	0.4817(2)	1.10288(16)	0.8794(3)	0.0909(8)
O3	0.73984(19)	0.82878(12)	0.32366(17)	0.0678(6)
O4	0.80060(16)	0.41631(11)	0.62719(17)	0.0555(5)
O5	0.89412(18)	0.27326(11)	0.4875(2)	0.0685(6)

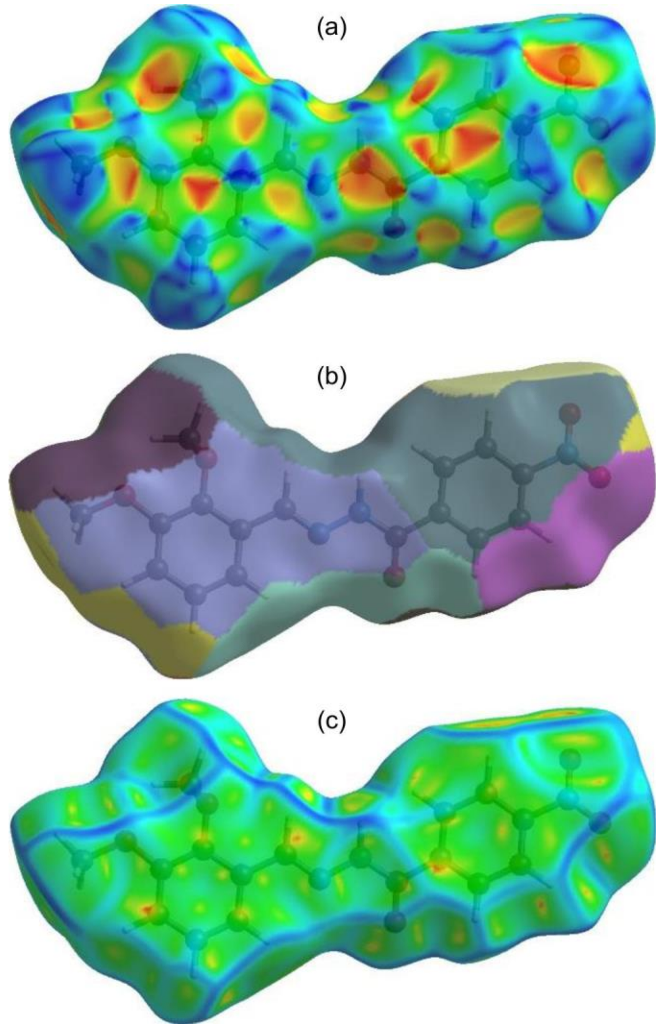

Fig. 6. (a) Shape index (b) fragment patch (c) curvedness image of DMNBH

interactions that contribute to overall stabilisation. The curvedness surface, characterised by flat green regions and deep blue grooves, reveals broad planar zones over the aromatic rings, reflecting the molecular planarity and efficient packing within the crystal. The combination of these features indicates that both hydrogen-bonding and π-stacking govern the supramolecular arrangement of DMNBH.

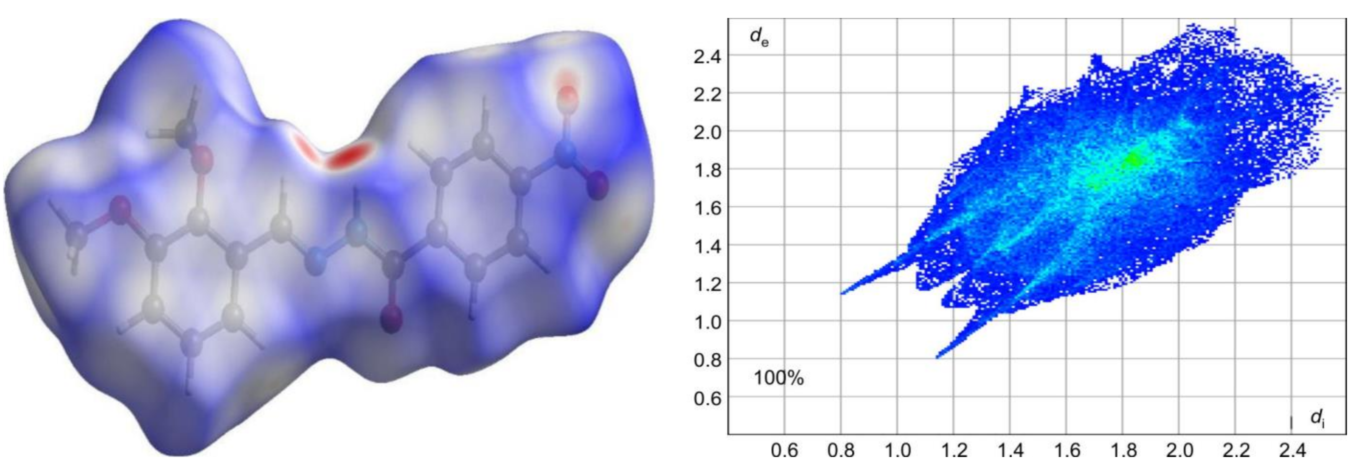

Fig. 5. (a) d_{norm} mapped surface and (b) overall 2D-plot of DMNBH

For a detailed comparison of the Hirshfeld-mapped surface, 2D-fingerprint plots (Fig. 7) were employed to calculate the contributions of specific atom-pair contacts. The analysis revealed that H···H interactions dominate the surface with 37.5%, reflecting the significant role of van der Waals forces in the crystal packing. The O···H/H···O interactions contribute 32.2%, confirming that these strong hydrogen-bonding contacts are the major stabilizing forces in the lattice. The N···H/H···N interactions account for 6.3%, while C···H/H···C (8.9%) and C···C (9.4%) contacts indicate the presence of weak C–H···π and π···π interactions between aromatic systems. Minor contributions such as C···O (2.1%), C···N (1.3%), O···N (1.3%) and O···O (1.1%) signify limited dipole–dipole and electrostatic interactions that further assist in structural stabilisation. Based on these results, these intermolecular forces stabilize the crystal structure and play a crucial role in influencing the optical and electronic properties DMNBH compound.

Energy framework: In the crystal packing of DMNBH, the pairwise intermolecular interaction energies were calculated using the energy-framework analysis to visualize the forces stabilizing the molecular crystal [33,34]. These energies were estimated for a nearest-neighbor cluster of molecules to evaluate the contributions of various interactions. To quantify this, a cluster with a radius of 3.8 Å was generated around the molecule and the energy calculations were performed. The calculated energies include electrostatic, polarisation, dispersion and exchange-repulsion components, allowing a detailed

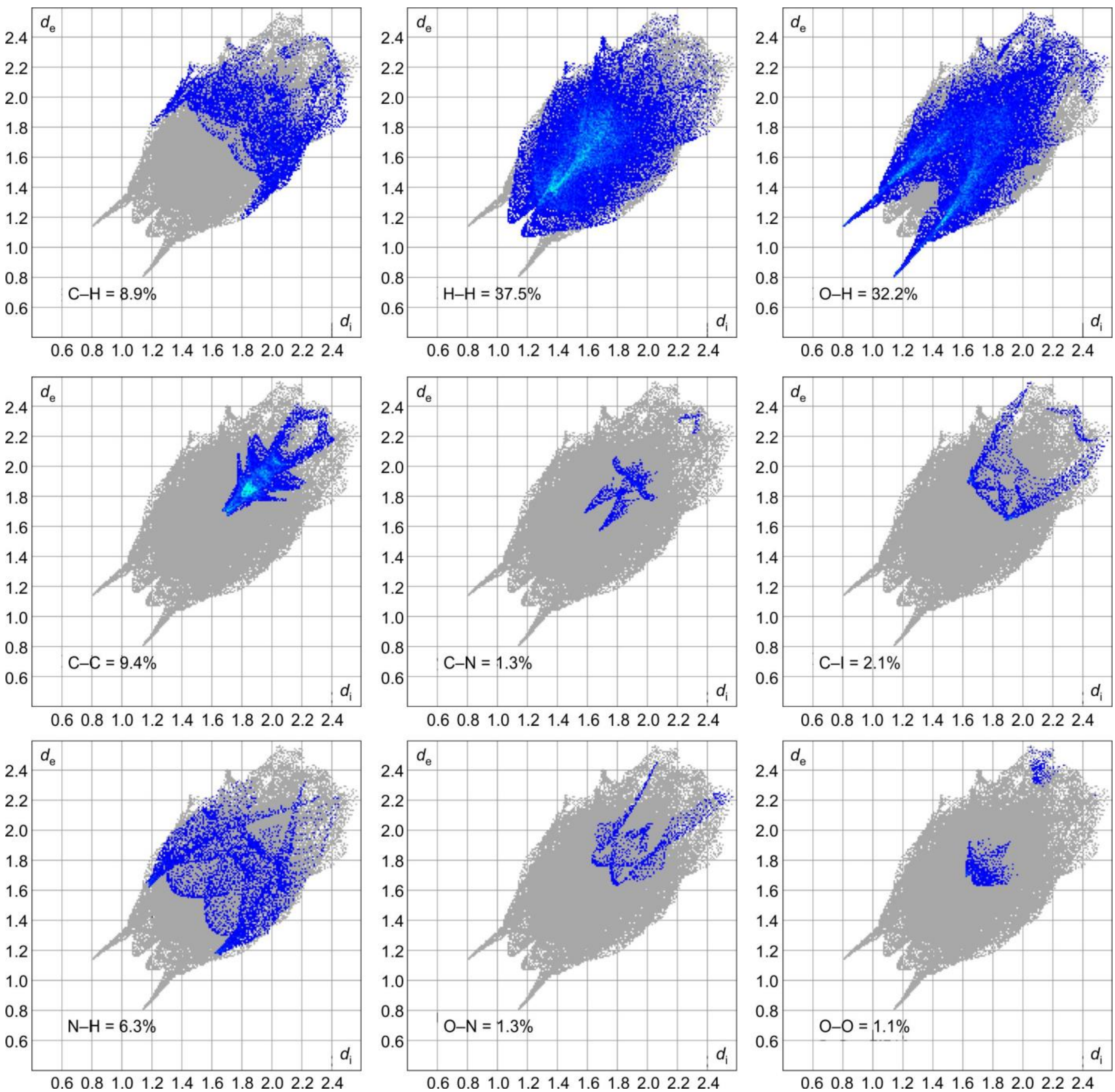

Fig. 7. 2D finger print plots of DMNBH

understanding of which interactions dominate the crystal stability. Fig. 8 shows a 3D views of these interactions, illustrating (dispersion, coulomb and total energy) their energetic significance maintaining the molecular arrangement. The nodes represent molecules, while the connecting cylinders indicate the strength of interactions, providing a quantitative visualisation of the forces stabilizing the crystal packing. From the calculated energy data (Table-6), it is evident that the dispersion interaction energy dominates the all stabilisation of the DMNBH crystal. The strongest pairwise interaction (E_{total} = –46.7 kJ mol^{-1}) arises mainly from the large dispersion (–53.1 kJ mol^{-1}) and electrostatic (–33.1 kJ mol^{-1}) contributions, partially counterbalanced by repulsive energy (42.5 kJ mol^{-1}). The next other significant interaction displays a total energy of –43.1 kJ mol^{-1}, again dominated by a substantial dispersion component (–59.6 kJ mol^{-1}). Several other intermolecular contacts, with total energies of –14.9, –13.0, –12.4 and –11.9 kJ mol^{-1}, provide additional stabilisation through moderate dispersion and weak electrostatic contributions. Taken together, these negative total interaction energies confirm that the crystal packing of DMNBH is energetically favourable and primarily stabilised by dispersion-dominated intermolecular forces, supplemented by moderate electrostatic and polarisation contributions. The variation in interaction magnitudes reflects the anisotropic distribution of forces throughout the lattice, ensuring the stability and compactness of the DMNBH crystal structure.

Molecular electrostatic potential (MEP): The MEP map of DMNBH molecule (Fig. 9) was computed at the B3LYP /6-311++G(d,p) level of theory to visualize the three-dimensional charge distribution and identify potential electrophilic and nucleophilic sites [35,36]. The surface topology of the

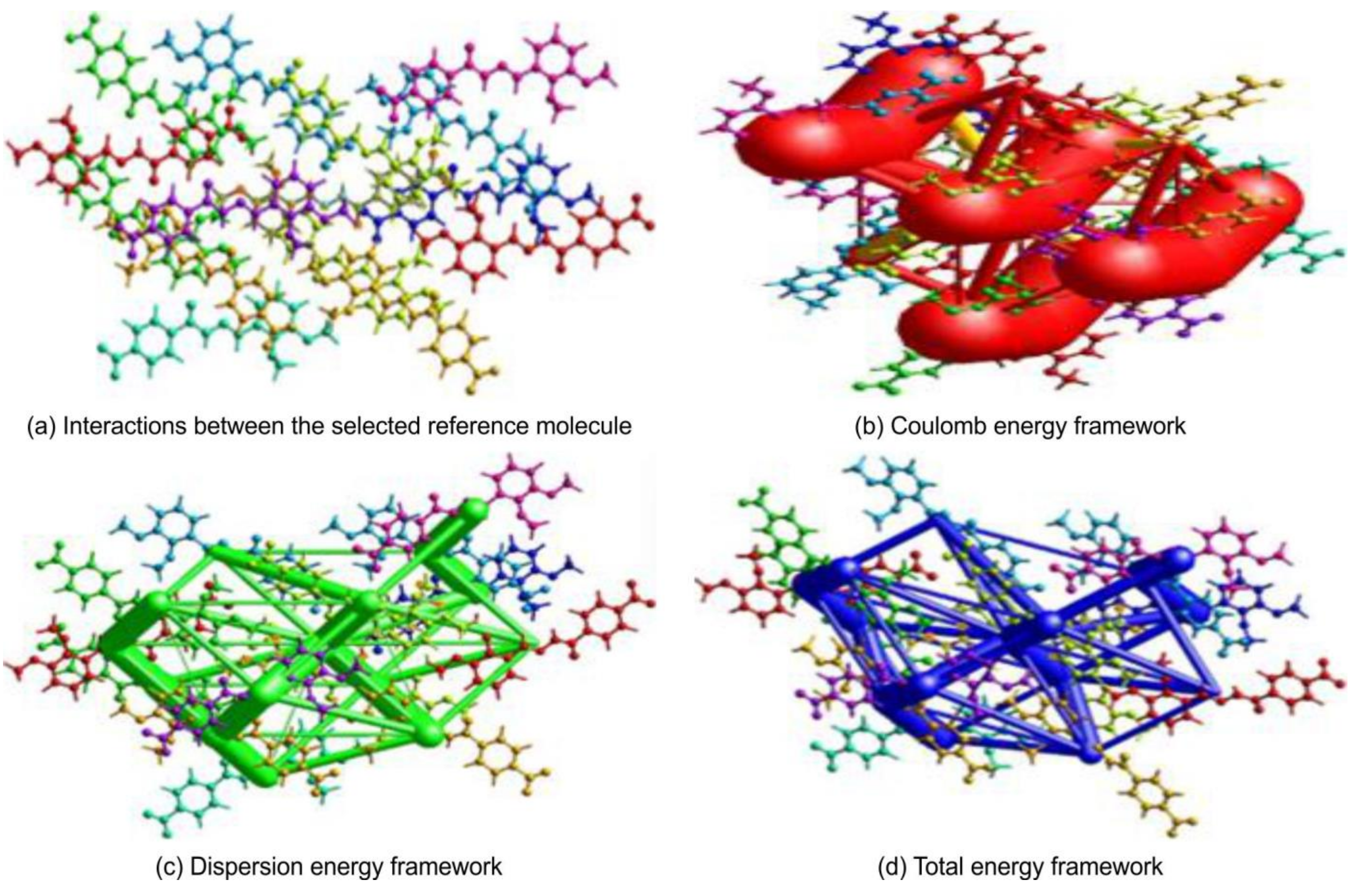

Fig. 8. Energy framework visualization of DMNBH

TABLE-6
INTERACTION ENERGIES (kJ mol^{-1}) FOR DMNBH BETWEEN A REFERENCE MOLECULE AND ITS NEIGHBOURS

N	Symop	R	E_ele	E_pol	E_dis	E_rep	E_tot
2	x, y, z	14.69	-1.6	-0.9	-9.4	2.9	-6.8
2	-x, y+1/2,-z+1/2	10.84	-2.3	-1.0	-15.4	6.3	-11.9
2	x,-y+1/2, z+1/2	4.81	-33.1	-10.9	-53.1	42.5	-46.7
2	x,-y+1/2, z+1/2	13.94	-5.2	-1.5	-20.3	9.7	-14.9
1	-x,-y,-z	12.89	-1.7	-0.2	-3.6	0.9	-4.4
2	-x, y+1/2,-z+1/2	10.18	-5.2	-2.3	-16.7	5.5	-12.4
1	-x,-y,-z	10.58	7.4	-1.7	-34.3	3.2	-25.2
1	-x,-y,-z	8.40	5.2	-2.3	-59.6	13.9	-43.1
1	-x,-y,-z	13.64	-11.3	-1.8	-7.4	3.9	-13.0

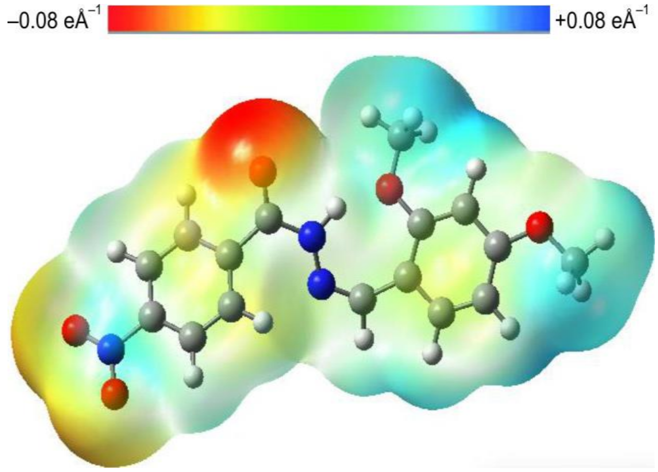

Fig. 9. Molecular electrostatical potential map of DMNBH

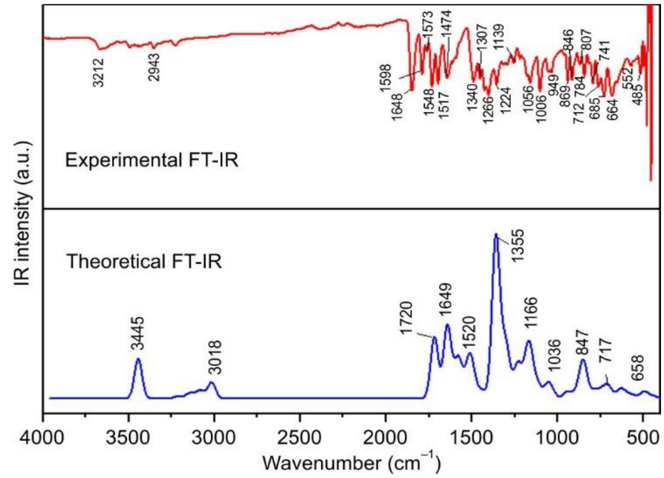

Fig. 10. (a) Experimental and (b) calculated FT-IR spectra of DMNBH

MEP closely reflects the electronic architecture of the optimised structure, clearly illustrating the influence of the $–NO_2$ and $–OCH_3$ substituents on the charge delocalisation. The colour-coded potential scale ranges from red (regions of highest electron density, negative potential) to blue (regions of lowest electron density, positive potential). Intense red regions around the carbonyl oxygen and nitro oxygen atoms denote strong electron-rich sites susceptible to electrophilic attack, while deep blue regions near the hydrazide N–H and azomethine hydrogen atoms indicate potential sites for nucleophilic interaction. The negative regions over the aromatic rings and methoxy oxygen atoms suggest their role in weak non-covalent stabilisation through intermolecular contacts. The continuous polarisation gradient observed across the hydrazone (–CONH–N=CH–) linkage demonstrates efficient intramolecular charge transfer (ICT) from the electron-donating methoxy group to the electron-withdrawing nitro group through the conjugated π-system. This electronic redistribution supports molecular planarity, stabilizes the crystal packing and significantly enhances the nonlinear optical (NLO) response of the DMNBH molecule.

Vibrations of DMNBH: The vibrational spectral assignments of DMNBH were analysed by comparing the experimental FT-IR spectrum and the theoretically computed spectrum at the B3LYP/6-311++G(d,p) level (Fig. 10). The close agreement between observed and calculated wavenumbers, confirms the accuracy of the theoretical approach. The characteristic vibrational modes such as N–H and C=N stretching, aromatic C=C skeletal vibrations and asymmetric/symmetric NO_2 modes, reflected the influence of functional groups on the molecular framework as detailed in Table-7.

N–H vibrations: In the hydrazone-containing DMNBH molecule, the presence of the –CONH–NH– moiety was confirmed through N–H vibrational modes. The N–H stretching vibration was observed as a strong peak at 3212 cm^{-1} in the experimental FT-IR spectrum and at 3324 cm^{-1} in the theoretical spectrum, which falls within the typical region of N–H stretching [37,38]. The corresponding N–H in-plane bending vibrations appeared as strong band at 1517 and 1474 cm^{-1} experimentally, with calculated DFT values at 1480 and 1467 cm^{-1}, confirming the contribution of the hydrazone group within the molecule.

Deformation of C–H/CH_3 vibrations: Methoxy groups attached to aromatic rings typically form a sharp and isolated C–H stretching vibration near 2835 cm^{-1} [39]. In DMNBH, this band appears experimentally at 2943 cm^{-1} and was calculated by DFT at 3012 cm^{-1}, indicating that the $–OCH_3$ group is affected by conjugation with the aromatic ring and interactions within the hydrogen-bonding network.

C=N/C–N vibrations: The presence of azomethine (C=N) and C–N linkages associated with hydrazone functionality is confirmed by characteristic vibrational bands in the FT-IR spectrum. The C=N stretching vibrations, arising from azomethine groups conjugated with the aromatic rings, are experimentally observed strong peak at 1648 and 1598 cm^{-1}, in good agreement with DFT-calculated values of 1659 and 1603 cm^{-1} [40]. The C–N stretching vibrations, which include contributions from secondary amine and methoxy-linked amine groups, appear at 1573, 1307 and 1056 cm^{-1}, closely matching the computed values of 1584, 1313 and cm^{-1}. The multiplicity and shifts of these bands reflect the influence of conjugation and varying chemical environments within the molecule.

C=O/C-O vibrations: The carbonyl (C=O) and ether/ester (C–O) groups in DMNBH were identified by their characteristic vibrational bands in the FT-IR spectrum. The C=O stretching vibration of the hydrazone-related carbonyl is observed strong peak experimentally at 1648 cm^{-1}, closely matching the DFT-calculated value of 1659 cm^{-1}, reflecting conjugation with the azomethine and aromatic rings [41]. The C–O stretching vibrations, associated with methoxy groups, occur experimentally at 1224 and 1006 cm^{-1}, in good agreement with DFT values of 1238 and 1007 cm^{-1}. These bands, consistent with typical IR characteristics, arise from differing chemical environments and conjugation effects within the molecule.

C–NO_2 vibrations: The nitro substituents display distinct vibrational modes in the infrared region due to the characteristic nature of the N–O and C–NO_2 bonds. In DMNBH, the C–NO_2 group exhibits FT-IR absorption bands at 1307 and 1056 cm^{-1}, corresponding to symmetric and asymmetric N–O stretching, with DFT values of 1313 and 1074 cm^{-1}, showing good agreement between experiment and theoretical results [42].

TABLE-7
THE B3LYP/6–311++G (d, p) CALCULATED FREQUENCIES (ν_{calc}), SCALED FREQUENCIES (ν_{sc}), MODE ASSIGNMENTS PED, EXPERIMENTAL FREQUENCIES FOR IR SPECTRUM (νexp.IR) AND ASSIGNMENTS FOR DMNBH (FREQUENCIES IN cm^{-1})

Unscaled frequency (cm^{-1})	Scaled frequency (cm^{-1})	IR intensity (a.u.)	Vib. mode No. (PED)	Exp. IR (cm^{-1})	Assignment descriptions
3445	3324	251.2	NH, s1, (100)	3212	N–H stretching (hydrazone group)
3122	3012	9.033	CH, s5, (99)	2943	C–H stretching (azomethine group) hydrazone linkage
1719	1659	389.5	CO, s16, (75)	1648	C=O stretching (Carbonyl group of benzohydrazide); C–N–H in-plane deformation (bending); C–C stretching (coupled with C=O and C=N)
1661	1603	8.046	CN, s17, (72)	1598	N–N stretching (coupled with N–H bending) (hydrazone group); C=N stretching (azomethine group); C–H stretching (azomethine group)
1645	1587	340.5	CC, s20, (12); CC, s21, (27); CC, s27, (14); CC, s28, (10)		C=C (2,4-dimethoxybenzylidene); C–H bending (2,4-dimethoxybenzylidene)
1641	1584	106.8	CCC, s61, (10); CC, s23, (30);	1573	C=C; C–H bending; C–N bending (4-nitrobenzohydrazide)
1637	1580	3.074	CC, s22, (11); CC, s25, (30); CC, s29, (10)		C=C; C–H bending(4-nitrobenzohydrazide)
1601	1545	84.3	CC, s26, (34); CC, s27, (12)	1548	C=C; C–H bending (2,4-dimethoxybenzylidene)
1534	1480	47.18	HNN, s41, (10); HCC, s43, (18) HCC, s44, (11)	1517	N–H bending (hydrazone group); C–H bending (2,4-dimethoxybenzylidene); C–H2 scissoring bendig (2,4-dimethoxybenzylidene); C-C strecthing (2,4-dimethoxybenzylidene)
1520	1467	3.104	HCC, s47, (16); HCC, s48, (15); HCC, s49, (17); HCC, s50, (15)	1474	N–H bending (hydrazone group); C-C strecthing; C–H bending (4-nitrobenzohydrazide)
1516	1463	142.6	CO, s16, (10); HNN, s41, (56)		N–H bending (hydrazone group); CH_3 bending (2,4-dimethoxybenzylidene)
1425	1375	2.668	HCN, s45, (50);	1340	C–H bending (2,4-dimethoxybenzylidene)
1361	1313	842.2	NO, s18, (19); NO, s19, (16); CN, s30, (17)	1307	NO_2 bending; C–N stretching; N–H bending; C–H bending (4-nitrobenzohydrazide)
1325	1279	2.357	CC, s29, (11); HCC, s47, (22); HCC, s48, (18); HCC, s49, (19); HCC, s50, (17)	1266	C–H bending (4-nitrobenzohydrazide)
1283	1238	92.96	HCC, s43, (28); CC, s27, (11); CO, s32, (12)	1224	C–H bending ((2,4-dimethoxybenzylidene); C-O stretching
1186	1144	119.7	HCOC, s86, (11); HCOC, s87, (11); HCC, s44, (11)	1139	CH_3 (2,4-dimethoxybenzylidene)
1113	1074	6.548	NN, s33, (11); CN, s38, (12); CC, s23, (16); CC, s24, (13)	1056	C–NO_2 strecthing; C-C stretching; C–H bending; C–N bending (4-nitrobenzohydrazide)
1066	1028	59.24	CO, s36, (49); HCC, s44, (10); CC, s26, (10); CC, s28, (12)		C-O strecthing; C-C stretching; C–H bending (2,4-dimethoxybenzylidene)
1043	1007	49.23	CO, s37, (57); CCC, s39, (12); CCC, s64, (11)	1006	C-O strecthing; C-C stretching; C–H bending (2,4-dimethoxybenzylidene)
988	953	0.774	HCCC, s82, (25); HCCN, s83, (39)	949	C–H bending (4-nitrobenzohydrazide)
905	873	8.883	HCNN, s80, (76)	869	C–H bending (2,4-dimethoxybenzylidene)
876	845	9.5	CC, s23, (10); ONO, s58, (37)	846	NO_2 sci bending; C-C stretching (4-nitrobenzohydrazide)
848	818	44.65	HCCC, s82, (28); HCCN, s83, (27); HCCC, s84, (15); HCCC, s85, (13)	807	C–H bending (4-nitrobenzohydrazide)
802	774	24.87	HCCC, s77, (56); HCCC, s78, (14); HCCC, s77(56)	784	C–H bending (2,4-dimethoxybenzylidene)
782	754	23.21	OCON, s106, (10); ONCC, s107, (40)		
773	746	10.86	CCC, s63, (12); HNNC, s76, (10)	741	ring vibration
738	712	14.53	HNNC, s76, (11); CC, s26, (14); CCC, s64, (13)	712	C-C-C sci.bending (2,4-dimethoxybenzylidene)
716	691	48.53	OCON, s106, (52)	685	C–N bending; No2 bending (4-nitrobenzohydrazide)
696	671	36.54	HNNC, s76, (24)	664	N-N–H bending (hydrazide)
577	557	3.998	CCC, s64, (14)	552	ring distortion
499	481	36.63	CC, s35, (10); NC, s38, (13); OCN, s56, (16)	485	ring distortion

UV-Visible spectroscopy: The UV-Vis spectral analysis of the DMNBH compound was carried out using both experimental (Fig. 11a) and theoretical TD-DFT (Fig. 11b) approaches to elucidate its electronic transition characteristics. In accordance with Beer-Lambert's law [43,44], the experimental UV-Visible absorption spectrum was recorded in the range of 280-800 nm, exhibiting a strong and broad absorption band centered at 295-310 nm, which was attributed to the $\pi \rightarrow \pi^*$ electron transition arising from the extended conjugation between the aromatic rings and the azomethine (C=N) linkage. This transition signifies extensive π-electron delocalisation over the benzylidene and hydrazide moieties, enhancing the transition probability and confirming the highly conjugated electronic framework of compound. The optical band gap energy derived from the Tauc's plot (Fig. 11a) was found to be 2.98 eV, supporting the presence of a small band gap and efficient π–π^* transition behaviour. In addition, a weak and gradually decaying tail extending up to 400 nm is observed, corresponding to a low-intensity $n \rightarrow \pi^*$ or intramolecular charge-transfer (ICT) transition. This feature originates from electron donation by the methoxy ($-OCH_3$) substituents to the electron-withdrawing nitro ($-NO_2$) group through the π-conjugated bridge, indicating partial charge redistribution within the molecule. In comparison, the TD-DFT simulated spectrum shows two absorption peaks at 310 nm and 405 nm. The intense peak around 310 nm is assigned to a HOMO →LUMO ($\pi \rightarrow \pi^*$) excitation, while the weaker transition near 405 nm corresponds to an $n \rightarrow \pi^*$ or ICT process involving donor–acceptor orbital interactions. The close agreement between the experimental and theoretical spectra confirms the reliability of the TD-DFT model, while minor variations arise from solvent and vibronic effects. Collectively, these findings demonstrate that DMNBH possesses an extended π-conjugated framework with partial intramolecular charge-transfer character, affirming its potential for nonlinear optical (NLO) and optoelectronic applications.

HOMO-LUMO orbital analysis: The HOMO-LUMO studies of DMNBH provide insight into its electronic structure, chemical reactivity and molecular stability, which arise from the intramolecular charge transfer (ICT) between donor and acceptor groups through the π-conjugated system [45,46]. The spatial distribution of the HOMO and LUMO orbitals (Fig. 12) maps the region involved in electron density transition within the molecule. In particular, HOMO lobes are primarily localised over the electron-rich aromatic ring and hydrazide linkage, whereas the LUMO is centered on the nitro-substituted aromatic region. This distinct separation of electron density confirms the presence of a strong donor–acceptor architecture in DMNBH.

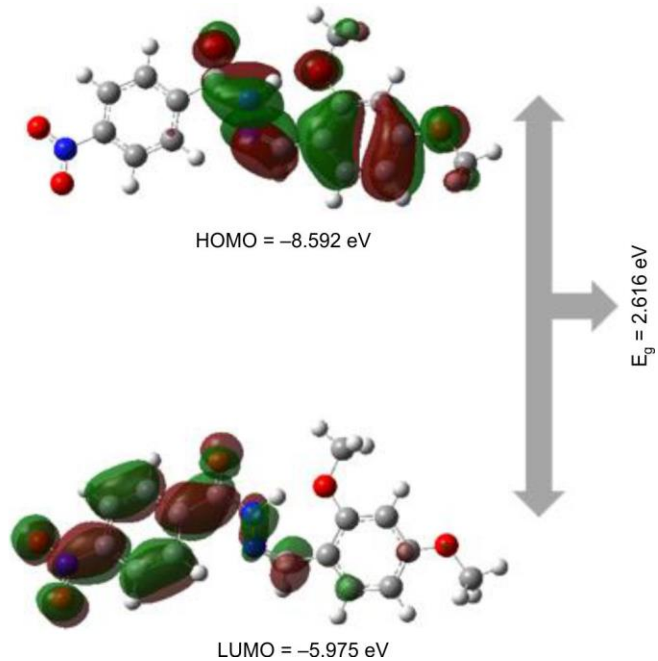

Fig. 12. HOMO-LUMO plot of DMNBH

The calculated HOMO (–8.592 eV) and LUMO (–5.9758 eV) energy levels correspond to a low energy gap of 2.616 eV, suggesting that taken molecule can be easily polarised and undergo electronic excitation with minimal energy. Such efficient charge transfer and polarizability are essential attri-

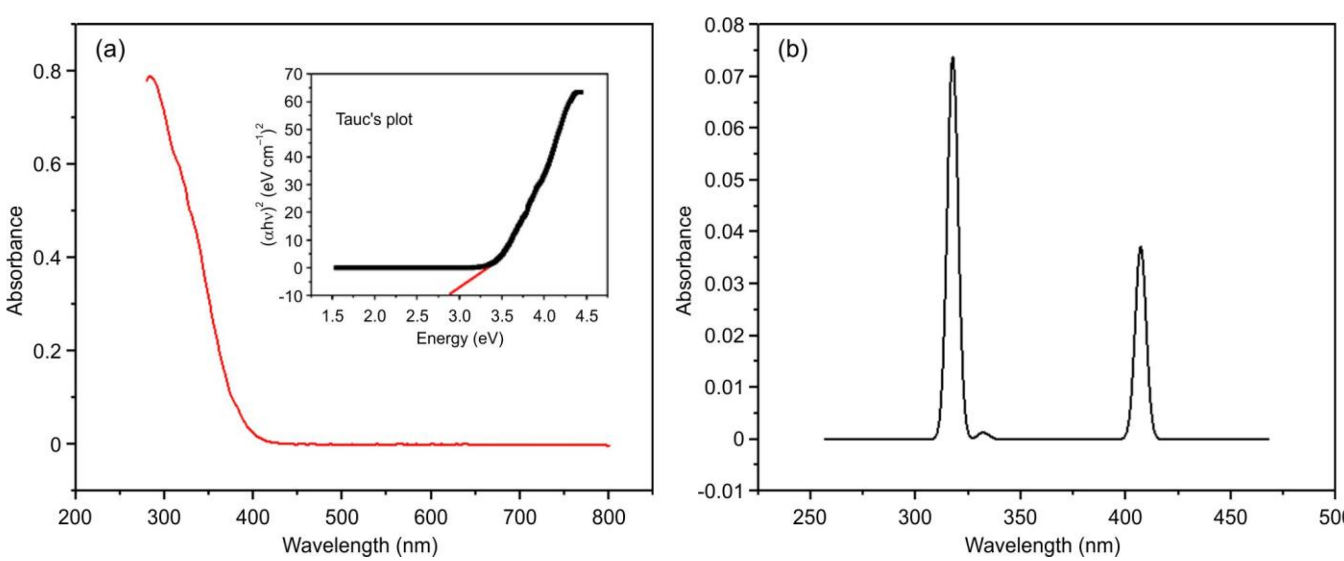

Fig. 11. (a) Experimental UV absorption and (b) calculated (TD-DFT) spectra of DMNBH

butes for materials intended for optoelectronic and nonlinear optical applications. This electronic configuration is further validated by the global reactivity descriptors, which provide deeper insight into the molecule's chemical behaviour as listed in Table-8. The ionization potential (I = 8.592 eV) and electron affinity (A = 5.976 eV) indicate that it has a balanced ability to both donate and accept electrons, while its relatively high electronegativity (χ = 7.284 eV) shows a strong tendency to attract electron density. The moderate global hardness (η = 1.308 eV) along with the corresponding global softness (S = 0.654 eV) indicate that DMNBH is chemically adaptable and easily polarizable. Additionally, the chemical potential (μ = –3.992 eV) and elevated global electrophilicity index (ω = 10.421 eV) highlight its capability to act as a potent electrophile, while the maximum electronic charge transfer (ΔN_{max} = 1.481 eV) confirms its significant ability to accept electron density from donor units. These features, along with its strong intramolecular charge transfer and high polarizability, establish DMNBH as a promising candidate for advanced optoelectronic and nonlinear optical applications.

TABLE-8
HOMO–LUMO ENERGY VALUE AND RELATED PROPERTIES OF DMNBH CALCULATED AT B3LYP/6–311++G (d, p) METHOD

Parameters	Formula	Gaseous phase (eV)
HOMO	E_{HOMO}	-8.592
LUMO	E_{LUMO}	-5.976
Energy gap ΔE	E_{HOMO}–E_{LUMO}	2.616
Ionisation potential (A)	–E_{HOMO}	8.592
Electron affinity (I)	–E_{LUMO}	5.976
Electronegativity (χ)	(I+A)/2	7.284
Global hardness (η)	(A-I)/2	1.308
Global softness (S)	1/2η	0.654
Chemical potential (μ)	–χ	-3.992
Global electrophilicity (ω)	$\mu^2/2\eta$	10.421
Maximum electronic charge (ΔN max)	–(μ/η)	1.481

NBO analysis: The NBO studies of DMNBH demonstrate that strong donor–acceptor interactions plays a crucial role in stabilizing the molecule through intra and intermolecular charge delocalisation. The stabilisation energy $E^{(2)}$, derived from second-order perturbation theory [47,48], quantify the strength of these interaction between filled (donor) and antibonding (acceptor) orbitals, leading to significant $\pi\rightarrow\pi^*$ and $n\rightarrow\pi^*$ delocalisations among the aromatic rings, which elucidate the extract and contribution of these interactions. The highest stabilisation energy is observed for the LP (3)-O21→π(N20–O22) interaction of 163.66 kcal/mol, arising from $n\rightarrow\pi^*$ delocalisation within the nitro group. This strong interaction reflects efficient electron transfer from the oxygen lone pair into the antibonding N–O orbital, indicating pronounced charge redistribution toward the –NO_2 group. The next major stabilisation involves LP (1)-N38→π(C10–O12) of 43.17 kcal/mol and LP (1)-N38→π(C8–N9) of 28.01 kcal/mol interactions, representing charge transfer from the hydrazide nitrogen toward the adjacent carbonyl and imine groups, confirming strong conjugation across the C=N–NH–CO linkage (Table-9). Among the aromatic systems, notable $\pi\rightarrow\pi^*$ interactions such as π(C16–C17)→π(N20–O22) of 27.61 kcal/mol, π(C1–C6)→π(C4–C5) of 27.28 kcal/mol and π(C2–C3)→π(C1–C6) of 25.52 kcal/mol demonstrate effective π-electron delocalisation across both the phenyl and nitro-substituted rings. These interactions enhance molecular stability and planarity through extended conjugation. Furthermore, LP (2)-O13→π(C1–C6) of 29.65 kcal/mol) and LP (2)-O7→π(C4–C5) of 26.14 kcal/mol indicate that the methoxy oxygen atoms donate electron density into the aromatic π-system, further strengthening conjugation within the DMNBH molecule. Thus, the NBO results confirm that the observed $\pi\rightarrow\pi^*$ and $n\rightarrow\pi^*$ interactions arise from strong conjugation between donor (–OCH_3, –NH–CO) and acceptor (–NO_2, C=O, C=N) groups, leading to efficient intramolecular charge transfer, enhanced electronic delocalisation and improved nonlinear optical (NLO) response.

TABLE-9
SECOND-ORDER PERTURBATION THEORY ANALYSIS OF THE FOCK MATRIX IN NBO BASIS CALCULATED AT B3LYP/6–311++G(d,p) LEVEL

Donor (i)	Acceptor (j)	E(2) (Kcal/mol)	E(j)-E(i) (a.u.)	F(i.j) (a.u)
π(C1-C6)	π*(C2-C3)	15.26	0.29	0.059
π(C1-C6)	π*(C4-C5)	27.28	0.28	0.08
π(C2-C3)	π*(C1-C6)	25.52	0.27	0.077
π(C2-C3)	π*(C4-C5)	14.45	0.28	0.059
π(C4-C5)	π*(C1-C6)	16.98	0.27	0.061
π(C4-C5)	π*(C2-C3)	25.37	0.28	0.076
π(C4-C5)	π*(C8-N9)	13.66	0.28	0.058
π(C11-C15)	π*(C10-O12)	14.52	0.3	0.06
π(C11-C15)	π*(C16-C17)	22.77	0.27	0.07
π(C11-C15)	π*(C18-C19)	19.15	0.28	0.068
π(C16-C17)	π*(C11-C15)	18.31	0.3	0.067
π(C16-C17)	π*(C18-C19)	19.08	0.3	0.069
π(C16-C17)	π*(N20-O22)	27.61	0.14	0.06
π(C18-C19)	π*(C11-C15)	20.24	0.29	0.069
π(C18-C19)	π*(C16-C17)	21.84	0.27	0.069
π(N20-O22)	LP(3)-O21	12.49	0.18	0.079
LP(2)-O7	π*(C4-C5)	26.14	0.35	0.093
LP(2)-O12	π*(C10-C11)	18.51	0.64	0.021
LP(2)-O12	π*(C10-N38)	23.65	0.69	0.116
LP(2)-O13	π*(C1-C6)	29.65	0.34	0.095
LP(3)-O21	π*(N20-O22)	163.66	0.14	0.139
LP (1)-N 38	π*(C8-N9)	28.01	0.29	0.084
LP (1)-N 38	π*(C10-O12)	43.17	0.31	0.106

First-order hyperpolazability: The quantum chemical evaluation of polarizability and hyperpolarizability provides a valuable insight into the linear and nonlinear optical (NLO) behaviour of the DMNBH molecule. By using the B3LYP/6-311++G(d,p) level of theory, the dipole moment, mean polarizability and first-order hyperpolarizability were computed to assess the potential for NLO applications of molecule [49,50]. The calculated dipole moment components (μ_x = 10.6564 D, μ_y = –0.6635 D, μ_z = –0.4805 D) give a total dipole moment of μ_{total} = 10.6878 D, indicating a strong ground-state polarity predominantly oriented along the x-axis and suggesting efficient intramolecular charge transfer (ICT) from the donor to acceptor moieties through the π-conjugated bridge. The mean polarizability (α_{tot} = 142.75 ×10^{-24} esu) and tensor components (α_{xx} = –153.2552, α_{yy} = –131.9454, α_{zz} = –143.0445) demonstrate high electronic deformability under an applied electric field, consistent with the delocalised π-electron framework of the molecule (Table-10). The first-order hyperpolarizability (β) tensor components show strong anisotropy, with the dominant contribution arising from β_{xxx} (612.8782 ×10^{-31} esu), while the other components, including β_{xxy} (35.9288), β_{xxz} (32.2244), β_{xyy} (82.1647), β_{xzz} (–7.3883), β_{yzz} (–3.3331), β_{yyz} (–18.2183), β_{xyz} (–0.0827), β_{yyy} (6.2523) and β_{zzz} (1.4279) ×10^{-31} esu, contribute less significant. The calculated total hyperpolarizability (β_{tot} = 688.924 ×10^{-31} esu) is approximately 184.7972 times greater than that of the urea molecule indicating an enhanced intrinsic molecular electronic polarisation and charge-transfer response. These results reflect molecular-level optical response and do not imply macroscopic second-order non-linear optical activity in the centrosymmetric crystal. Compared with the related π-conjugated systems such as (*E*)-*N′*-(2,4-dimethoxybenzylidene)benzohydrazide [20] (eight times greater than urea) and (*E*)-4-bromo-*N′*-(2,4-dimethoxybenzylidene)-benzohydrazide [51] (six times greater than urea), DMNBH shows an favourable NLO response due to its efficient donor–acceptor substitution and enhanced hydrazone-linked conjugation. These molecular properties may be relevant for understanding electronic and optical response in the related systems.

TABLE-10
FIRST ORDER HYPERPOLARIZABILITY DATA OF DMNBH

Parameters	B3LYP/ 6-311++G (d,p)	Parameters	B3LYP/ 6-311++G (d,p)
μ_x	10.6564	β_{xxx}	612.8782
μ_y	-0.6635	β_{yyy}	6.2523
μ_z	-0.4805	β_{zzz}	1.4279
μ_{tot}	10.6878	β_{xyy}	82.1647
α_{xx}	-153.2552	β_{xxy}	35.9288
α_{yy}	-131.9454	β_{xxz}	32.2244
α_{zz}	-143.0445	β_{xzz}	-7.3883
α_{xy}	-16.1733	β_{yzz}	-3.3331
α_{xz}	1.1682	β_{yyz}	-18.2183
α_{yz}	-5.7776	β_{xyz}	-0.0827
α_{tot} (esu) × 10^{-24}	-142.7483	β_{tot}(esu) × 10^{-31}	688.924
		Urea × 10^{-31}	184.7972

Molecular docking studies: To elucidate the molecular interaction behaviour and possible biological relevance of the DMNBH molecule, docking studies were carried out as a preliminary *in silico* approach to understand its binding preference and interaction pattern within the active site of the selected target protein (PDB ID: 2IOK) [52,53]. Molecular docking was performed using AutoDock [29] to evaluate the binding affinity and interaction stability between DMNBH and the protein. The optimised geometry of DMNBH obtained from GaussView was used as the ligand, while the receptor was prepared by removing water molecules, adding hydrogen atoms and assigning Kollman charges. The resulting docked complexes were analysed and visualised in PyMOL [30] to identify key amino acid residues involved in the binding interactions. Fig. 13a depicts the binding pocket and the best docking pose of DMNBH, corresponding to the most favourable binding score. The DMNBH molecule exhibited a binding affinity of –6.33 kcal mol^{-1}, suggesting a strong and stable interaction within the active-site cavity of 2IOK. The heterocyclic hydrazone core of DMNBH enables directional interactions and a crucial hydrogen bond formed with HIS524 plays a key role in anchoring the ligand and stabilizing its orientation (Fig. 13b). The extended π-conjugated framework of DMNBH, possessing moderate polarizability, interacts effectively with the surrounding hydrophobic residues, forming van der Waals and alkyl contacts with LEU384, LEU387,

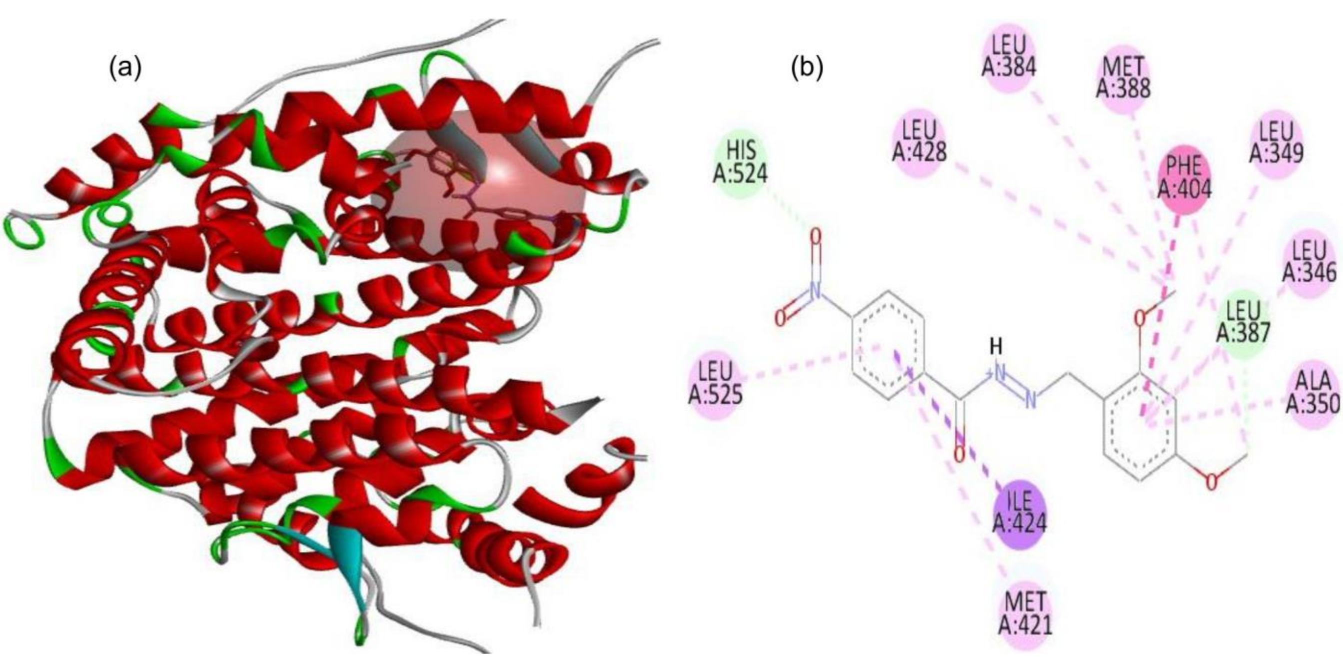

Fig. 13. (a) Binding energy and (b) hydrogen-hydrophobic interactions of 2IOK protein

LEU346, LEU349, LEU428, LEU525, MET388, MET421, ILE424 and ALA350, which collectively contribute to the compact stabilisation of the complex. Moreover, PHE404 establishes π–π and π–alkyl interactions with the aromatic ring of DMNBH, reinforcing the overall binding stability through aromatic stacking and dispersion effects. The combined network of polar and nonpolar interactions indicates that DMNBH exhibits strong molecular recognition and affinity toward the 2IOK receptor. Further, highlighting a qualitative ligand-protein interaction and the structural adaptability of the molecule providing preliminary insight into its molecular recognition behaviour and suggesting possible relevance for cancer-related studies, subject to further experimental validation.

Conclusion

A new organic single crystal of DMNBH compound has been successfully grown by slow evaporation method and characterised through both experimental and theoretical methods. Single-crystal X-ray diffraction revealed that DMNBH crystallizes in the monoclinic crystal system with space group $P2_1/c$, stabilised by N–H···O and C–H···O hydrogen bonds along with π–π stacking interactions. FT-IR spectra confirmed the presence of the azomethine (C=N) band at 1648 cm^{-1} and nitro vibrations at 1307 and 1056 cm^{-1}, while UV-Vis spectra exhibited $\pi\rightarrow\pi^*$ and $n\rightarrow\pi^*$ transitions characteristic of the donor–acceptor systems. DFT calculations at the B3LYP/6-311++G(d,p) level showed good agreement with experimental data and revealed a HOMO–LUMO energy gap of 2.616 eV, indicating low chemical reactivity and high charge transfer efficiency. NBO analysis demonstrated significant delocalisation of electron density from lone pairs of oxygen atoms to antibonding orbitals, contributing to molecular stabilisation. Hirshfeld surface and energy framework analyses highlighted the major role of O···H and C···H contacts in the crystal packing. The calculated first-order hyperpolarizability value confirmed notable nonlinear optical (NLO) behaviour. Furthermore, molecular docking studies indicated favourable binding interactions (–6.35 kcal mol^{-1}) of DMNBH with the target protein, suggesting potential bioactive properties. Thus, the results obtained from experimental investigations, theoretical calculations and molecular docking studies collectively highlight the potential of DMNBH for optoelectronic and biological applications.

Supporting information

CCDC No. 2376542 contains the supplementary crystallographic data for the synthesized DMNBH hydrazone derivative. These data can be obtained free of charge from the Cambridge Crystallographic Data Centre (CCDC) *via* https://www.ccdc.cam.ac.uk/structures or by contacting CCDC, 12 Union Road, Cambridge CB2 1EZ, UK (fax: +44 1223 336033; e-mail: deposit@ccdc.cam.ac.uk

ACKNOWLEDGEMENTS

The authors acknowledge Marudhar Kesari Jain College for Women (Autonomous), Vaniyambadi, India, for using the computational lab in Fist instrumentation Lab (under Grant No. SR/FST/COLLEGE/2023/1511, FIST Program-2023 TPN-88688).

CONFLICT OF INTEREST

The authors declare that there is no conflict of interests regarding the publication of this article.

DECLARATION OF AI-ASSISTED TECHNOLOGIES

During the preparation of this manuscript, the authors used an AI-assisted tool(s) to improve the language. The authors reviewed and edited the content and take full responsibility for the published work.

REFERENCES

1. K. Erden, D. Soyler, A. Barsella, O. Şahin, S. Soylemez and Ç. Dengiz, *J. Org. Chem.*, **89**, 13192 (2024); https://doi.org/10.1021/acs.joc.4c01328
2. M. Haroon, T. Akhtar, Q.-U.-A. Shaikh, H. Mehmood, M. Khalid, M.A. Asghar, S.M. Alshehri and S.C. Ojha, *ACS Omega*, **8**, 27488 (2023); https://doi.org/10.1021/acsomega.3c03088
3. M.A. Assiri, A. Ali, M. Ibrahim, M.U. Khan, K. Ahmed, M.S.H. Akash, M.A. Abbas, A. Javed, M. Suleman, M. Khalid and I. Hussain, *RSC Adv.*, **13**, 21793 (2023); https://doi.org/10.1039/D3RA02433D
4. K. Naseema, K.V. Sujith, K.B. Manjunatha, B. Kalluraya, G. Umesh and V. Rao, *Opt. Laser Technol.*, **42**, 741 (2010); https://doi.org/10.1016/j.optlastec.2009.11.019
5. L. Kamath, A.P. Menezes, R. Bairy, S.K. Kumara swamy and A. Jayarama, *J. Mol. Struct.*, **1245**, 131019 (2021); https://doi.org/10.1016/j.molstruc.2021.131019
6. M. Haroon, T. Akhtar, M. Khalid, H. Mehmood, A.A.C. Braga, N. Alhokbany and S. Ahmed, *ChemistrySelect*, **8**, e202301209 (2023); https://doi.org/10.1002/slct.202301209
7. R.R. Ezz Eldin, M.A. Saleh, M.H. Alotaibi, R.K. Alsuair, Y.A. Alzahrani, F.A. Alshehri, A.F. Mohamed, S.M. Hafez, A.A. Althoqapy, S.K. Khirala, M.M. Amin, Y. A. F, A.H. AbdElwahab, M.S. Alesawy, A.A. Elmaaty and A.A. Al-Karmalawy, *J. Enzyme Inhib. Med. Chem.*, **37**, 1098 (2022); https://doi.org/10.1080/14756366.2022.2063282
8. S. Sultana, A. Akramullazi, M.F. Hossen, M.A. Asraf and M.K.-E. Zahan, *Mediterr. J. Chem.*, **14**, 122 (2024); https://doi.org/10.13171/mjc02407261780zahan
9. K.-H. Lee, F. Abas, N.B.M. Alitheen, K. Shaari, N.H. Lajis and S. Ahmad, *Molecules*, **16**, 9728 (2011); https://doi.org/10.3390/molecules16119728
10. C.J. Ezeorah, L.C. Ekowo, S.I. Eze, T. Groutso, S. Atiga, S.N. Okafor, N.N. Ukwueze and O.C. Okpareke, *J. Mol. Struct.*, **1270**, 133902 (2022); https://doi.org/10.1016/j.molstruc.2022.133902
11. Y. Yao, H.-L. Xu, Y.-Q. Qiu and Z.-M. Su, *J. Mol. Liq.*, **327**, 114882 (2021); https://doi.org/10.1016/j.molliq.2020.114882
12. X. Su and I. Aprahamian, *Chem. Soc. Rev.*, **43**, 1963 (2014); https://doi.org/10.1039/c3cs60385g
13. K. Naseema, V. Rao, K.V. Sujith and B. Kalluraya, *Curr. Appl. Phys.*, **10**, 1236 (2010); https://doi.org/10.1016/j.cap.2010.02.050
14. H.M. Robert, D. Usha, M. Amalanathan, R.R.J. Geetha and M.S.M. Mary, *J. Mol. Struct.*, 128948 (2020); https://doi.org/10.1016/j.molstruc.2020.128948
15. X. Zhao and Z.-T. Li, *Chem. Commun.*, **46**, 1601 (2010); https://doi.org/10.1039/B924552A
16. C. Zhang, X. Li, Y. Wang, M. An and Z. Sun, *J. Mater. Chem. C*, **9**, 11306 (2021); https://doi.org/10.1039/D1TC02434E
17. N. Kausar, S. Murtaza, M.N. Arshad, R. Rashid, A.M. Asiri, N. Javid, M.H. Asim and Z. Ashraf, *J. Mol. Struct.*, **1210**, 128042 (2020); https://doi.org/10.1016/j.molstruc.2020.128042

18. H.A. Katouah, J.H. Al-Fahemi, M.G. Elghalban, F.A. Saad, I.A. Althagafi, N.M. El-Metwaly and A.M. Khedr, *Mater. Sci. Eng. C*, **96**, 740 (2019); https://doi.org/10.1016/j.msec.2018.11.034
19. M.M. Barqi, A. Ashar, Z.A. Bhutta, M. Javed, I.M. Abdellah and M.R. Eletmany, *Int. J. Chem. Biochem. Sci.*, **24**, 369 (2023).
20. V. Saraswathi, S. Agilan, N. Muthukumarasamy, V.K. Gupta, M. Suresh, P. Peulakumari and D. Velauthapillai, *Opt. Quantum Electron.*, **54**, 758 (2022); https://doi.org/10.1007/s11082-022-04105-9
21. P. Jeeva, D. Barathi, R. Mani, A.D. Stephen, M. Louhi-Kultanen, G. Vinitha and A.G. Al-Sehemi, *J. Mol. Struct.*, **1254**, 132375 (2022); https://doi.org/10.1016/j.molstruc.2022.132375
22. C. Arunagiri, A.G. Anitha, A. Subashini and S. Selvakumar, *J. Mol. Struct.*, **1163**, 368 (2018); https://doi.org/10.1016/j.molstruc.2018.03.023
23. G.M. Sheldrick, SHELXL, Program for Crystal Structure Refinement, University of Gottingen, Germany, 1993.
24. G.M. Sheldrick, *Acta Crystallogr. A*, **64**, 112 (2008); https://doi.org/10.1107/S0108767307043930
25. M.J. Frisch, G.W. Trucks, H.B. Schlegel, G.E. Scuseria, M.A. Robb, J.R. Cheeseman, G. Scalmani, V. Barone, B. Mennucci, G.A. Petersson, H. Nakatsuji, M. Caricato, X. Li, H.P. Hratchian, A.F. Izmaylov, J. Bloino, G. Zheng, J.L. Sonnenberg, M. Hada, M. Ehara, K. Toyota, R. Fukuda, J. Hasegawa, M. Ishida, T. Nakajima, Y. Honda, O. Kitao, H. Nakai, T. Vreven, J.A. Montgomery Jr., J.E. Peralta, F. Ogliaro, M. Bearpark, J.J. Heyd, E. Brothers, K.N. Kudin, V.N. Staroverov, T. Keith, R. Kobayashi, J. Normand, K. Raghavachari, A. Rendell, J.C. Burant, S.S. Iyengar, J. Tomasi, M. Cossi, N. Rega, J.M. Millam, M. Klene, J.E. Knox, J.B. Cross, V. Bakken, C. Adamo, J. Jaramillo, R. Gomperts, R.E. Stratmann, O. Yazyev, A.J. Austin, R. Cammi, C. Pomelli, J.W. Ochterski, R.L. Martin, K. Morokuma, V.G. Zakrzewski, G.A. Voth, P. Salvador, J.J. Dannenberg, S. Dapprich, A.D. Daniels, O. Farkas, J.B. Foresman, J.V. Ortiz, J. Cioslowski and D.J. Fox, Gaussian16, Revision B.01, Gaussian, Inc., Wallingford, CT (2016).
26. M.H. Jamróz, *Spectrochim. Acta A Mol. Biomol. Spectrosc.*, **114**, 220 (2013); https://doi.org/10.1016/j.saa.2013.05.096
27. R. Dennington, T. Keith and J. Millam, GaussView, Version 5, Shawnee Mission, KS, USA: Semichem Inc. (2009).
28. S.K. Wolff, D.J. Grimwood, J.J. McKinnon, M.J. Turner, D. Jayatilaka, M. A. Spackman, Crystal Explorer, University of Western Australia, Version 3.1 (2012).
29. O. Trott and A.J. Olson, *J. Comput. Chem.*, **31**, 455 (2010); https://doi.org/10.1002/jcc.21334
30. L. Schrodinger and W. DeLano, PyMOL (2020).
31. A.M. Spackman and D. Jayatilaka, *CrystEngComm*, **11**, 19 (2009); https://doi.org/10.1039/B818330A
32. M.A. Spackman and J.J. McKinnon, *CrystEngComm*, **4**, 378 (2002); https://doi.org/10.1039/B203191B
33. M.J. Turner, S.P. Thomas, M.W. Shi, D. Jayatilaka and M.A. Spackman, *Chem. Commun.*, **51**, 3735 (2015); https://doi.org/10.1039/C4CC09074H
34. C.F. Mackenzie, P.R. Spackman, D. Jayatilaka and M.A. Spackman, *IUCrJ*, **4**, 575 (2017); https://doi.org/10.1107/S205225251700848X
35. V. Vijayalakshmi, G. Suresh, S. Thennarasu, K. Sukumar, J. Janczak, P. Revathi and N. Kanagathara, *J. Indian Chem. Soc.*, **102**, 102019 (2025); https://doi.org/10.1016/j.jics.2025.102019
36. E. Mohanapriya, N. Kanagathara, J. Janczak, M.K. Marchewka, S. Thennarasu, K. Sukumar and B. Praveena, *J. Mol. Struct.*, **1340**, 142479 (2025); https://doi.org/10.1016/j.molstruc.2025.142479
37. V. Vimalraj, S. Vijayalakshmi, S. Umayaparvathi and A.R. Krishnan, *Spectrochim. Acta A Mol. Biomol. Spectrosc.*, **78**, 670 (2011); https://doi.org/10.1016/j.saa.2010.11.045
38. A. Zülfikaroğlu, H. Batı and N. Dege, *J. Mol. Struct.*, **1162**, 125 (2018); https://doi.org/10.1016/j.molstruc.2018.02.079
39. N.B. Colthup, Introduction to Infrared and Raman Spectroscopy: Ethers, Alcohols and Phenols, Academic Press, pp. 327-337 (1990). https://doi.org/10.1016/B978-0-08-091740-5.50013-2
40. R. Gandhimathi and R. Dhanasekaran, *Optik*, **125**, 2912 (2014); https://doi.org/10.1016/j.ijleo.2013.11.040
41. S. Selvaraj, P. Rajkumar, M. Kesavan, K. Thirunavukkarasu, S. Gunasekaran, N.S. Devi and S. Kumaresan, *Spectrochim. Acta A Mol. Biomol. Spectrosc.*, **224**, 117449 (2020); https://doi.org/10.1016/j.saa.2019.117449
42. R.W. Beal and T.B. Brill, *Appl. Spectrosc.*, **59**, 1194 (2005); https://doi.org/10.1366/000370205774430873
43. K. Gandhi, N. Sharma, P.B. Gautam, R. Sharma, B. Mann and V. Pandey, Spectroscopy, in: Advanced Analytical Techniques in Dairy Chemistry, Springer US, New York, pp. 161-176 (2022).
44. M.S.H. Akash and K. Rehman, Ultraviolet–Visible (UV–VIS) spectroscopy, In: Essentials of Pharmaceutical Analysis, Springer, Singapore, pp. 29-42 (2020).
45. S. Selvaraj, A. Ram Kumar, A.S. Vickram, G.P. Sheeja Mol, M. Thirunavukkarasu and M. Kumar, *Int. J. Appl. Sci. Eng.*, **22**, 1 (2025); https://doi.org/10.6703/IJASE.202503_22(1).005
46. M. Buvaneswari, R. Santhakumari, C. Usha, R. Jayasree and S. Sagadevan, *J. Mol. Struct.*, **1243**, 130856 (2021); https://doi.org/10.1016/j.molstruc.2021.130856
47. A.R. Kumar, S. Selvaraj, M. Azam, G.P. Sheeja Mol, N. Kanagathara, M. Alam and P. Jayaprakash, *ACS Omega*, **16**, 31548 (2023); https://doi.org/10.1021/acsomega.3c04922.
48. C. Karnan and S. Selvaraj, *Int. Res. J. Multidiscip. Technov.*, **6**, 32 (2024); https://doi.org/10.54392/irjmt2444
49. R. Kaliammal, S. Sudhahar, G. Parvathy, K. Sankaranarayanan and K. Velsankar *J. Mol. Struct.*, **1212**, 128069 (2020); https://doi.org/10.1016/j.molstruc.2020.128069
50. B.S. Lakshmi, V. Sabari, E. Mohanapriya, K. Sukumar, M.K. Marchewka, J. Janczak and N. Kanagathara, *J. Mol. Struct.*, **1350**, 143894 (2026); https://doi.org/10.1016/j.molstruc.2025.143894
51. V. Saraswathi, S. Agilan, N. Muthukumarasamy, M. Uthayakumar, D. Velauthapillai and G. Vinitha, *J. Mater. Sci. Mater. Electron.*, **33**, 7883 (2022); https://doi.org/10.1007/s10854-022-07938-y
52. S. Ramkumar and R. Rajalakshmi, *Mater. Today Proc.*, (2023); https://doi.org/10.1016/j.matpr.2023.05.638
53. N. Kanagathara, G. Dhanalakshmi, E. Mohanapriya, P. Manikandan, A.K. Mohanakrishnan, V. Sabari, D. Vincy, V. Ragavendran and S. Aravindhan, *J. Mol. Struct.*, **1330**, 141347 (2025); https://doi.org/10.1016/j.molstruc.2025.141347